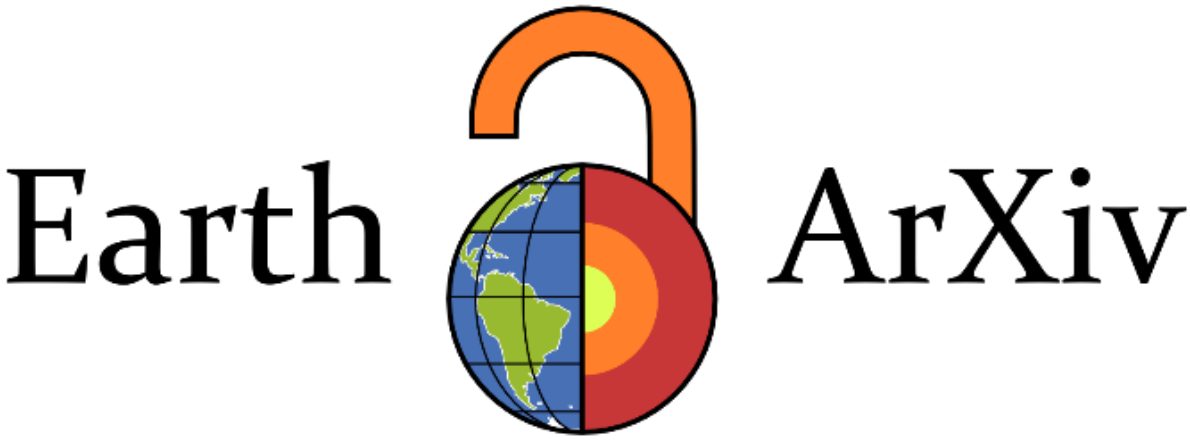

Manganese Oxidation States Reveal a Continental-Scale Climate-Driven Redox Gradient in Upland Soils

Ke Wen[1,2], Eric W. Slessarev[3], Oliver A. Chadwick[4], Aaron Thompson[5], Hongfei Liu[6], and Mengqiang Zhu[1,6]*

[1]Department of Ecosystem Science and Management, University of Wyoming, Laramie, WY 82071, USA

[2]State Key Laboratory of Deep Earth Processes and Resources, Guangzhou Institute of Geochemistry, Chinese Academy of Sciences, Guangzhou 510640, China

[3]Department of Ecology and Evolutionary Biology, Yale University, New Haven, CT 06511, USA

[4]Department of Geography, University of California, Santa Barbara, CA 93106, USA

[5]Department of Crop and Soil Sciences, University of Georgia, Athens, GA 40602, USA

[6]Department of Geological, Environmental and Planetary Sciences, University of Maryland, College Park, MD 20742, USA

*Corresponding author. E-mail address: mqzhu@umd.edu (M. Zhu)

Abstract

Soil redox conditions regulate soil organic carbon (SOC) persistence and nutrient availability, yet macroclimatic controls in uplands remain unclear because O_2 depletion reflects the interactions of moisture, labile carbon, soil texture, and microbial demand. Here we pair manganese (Mn) oxidation state, an integrative redox proxy, with effective water balance (mean annual precipitation minus potential evapotranspiration; MAP–PET) across mineral soils from 20 US ecoclimatic domains. Mn oxidation states shift predictably with MAP–PET: Mn(IV) dominates when MAP–PET < –1 m, Mn(III) at intermediate values (–1 to +1 m), and Mn(II) when MAP–PET > +1 m. These thresholds define a net average oxic–suboxic–anoxic continuum governed mainly by SOC concentration and water availability. Global extrapolation suggests suboxic uplands, the most prevalent state, store 78 – 91% of SOC, highlighting widespread oxygen limitation as a key stabilization mechanism across most upland ecosystems. Incorporating climate-driven redox thresholds into Earth system models should improve carbon–climate feedback predictions under rising hydroclimatic variability.

Main

The redox condition of soils critically influences ecosystem function and productivity through feedbacks amongst soil organic carbon (SOC), nutrients, contaminants, and the microbial community structure and activity[1–7]. Consequently, redox conditions have a large effect on terrestrial C cycle[1]. While substantial insights have been gained by viewing perennially saturated environments, particularly wetlands, through a redox lens, redox status has been less useful in upland terrestrial ecosystems. This gap primarily arises due to the technical challenges in reliably

measuring the mixed redox potential (E_h) in relatively dry and often coarse-textured upland soils[8], thereby constraining our understanding of carbon and nutrient dynamics in these systems.

Climate influences soil redox conditions in upland terrestrial ecosystems through its modulation of major soil variables, including direct impacts on soil moisture and temperature, as well as indirect impacts on pedogenesis that affect soil texture, SOC content, and microbial activity[7,9–11]. Among these, SOC and soil moisture exert the greatest control of soil redox status. Microbial decomposition of SOC consumes O_2 in soils whereas moisture hinders atmospheric O_2 diffusion into the soil. If O_2 supply cannot meet O_2 demand, anoxic soil conditions develop, emerging first in microaggregates or microsites due to the strong resistance to O_2 diffusion[5,12]. Although soil moisture and redox conditions in upland soils fluctuate temporally due to weather events, climate primarily shapes long-term average redox conditions. For instance, arid ecosystems typically maintain oxic conditions, whereas humid environments promote more reducing conditions. This climatic influence on soil redox has been demonstrated more quantitatively at the regional scale. Along a well-defined precipitation gradient with mean annual precipitation (MAP) ranging from 1.5 to 5 m on Maui Island, Hawaii, Schuur et al.[7] reported increasingly reducing conditions in clayey volcanic forest soils as MAP increased, despite significant temporal variability. The median redox potential (E_{h7}, i.e., E_h at pH 7) gradually decreased from E_{h7} values of 600 mV to 50 mV with increasing MAP, suggesting a shift of the characteristic soil redox conditions from oxic ($E_{h7} > 400$ mV) to suboxic ($E_{h7} = 400 – 300$ mV) and to anoxic ($E_{h7} < 300$ mV)[7]. However, this measured relationship between climatic factors and redox conditions has not been tested at broader, continental scales, where soils and vegetation vary remarkably.

The redox chemistry of manganese (Mn), existing as Mn(II), Mn(III), and Mn(IV) in soils[14], offers a powerful proxy for evaluating characteristic redox conditions of bulk soils in upland

terrestrial ecosystems. Manganese is actively cycled across all three soil redox zones[13–15], but its reactions are slow enough to preserve a buffered signal of local average redox conditions[13]. Mn(IV)-oxide-coated PVC films have been successfully used as redox indicators for reducing conditions in wetlands where they undergo reductive dissolution to Mn(II)[16]. Mn redox chemistry also holds significant promise for use as a redox proxy in upland soils because indigenous Mn oxidation states correlate closely with redox conditions[13,17,18]. As the characteristic soil redox conditions shifted from oxic, to suboxic, and to anoxic across the Maui and Kohala rainfall/redox gradients in Hawaii, the proportions of Mn(IV) and Mn(II) in the overall total Mn pool decreased and increased, respectively, whereas Mn(III) accumulated substantially in soils with prevalent suboxic conditions at intermediate MAP[13,18]. Such patterns closely parallel those in aquatic environments where dissolved Mn(III)-ligand complexes peak in the suboxic range[14,15,19]. Although soil pH also influences Mn speciation, consistent pH conditions across the Maui gradient (pH ~4) attribute the observed variations primarily to redox shifts rather than pH effects.

Here, we define climatic thresholds that differentiate oxic, suboxic, and anoxic soil redox regimes at a continental scale by analyzing Mn oxidation states across diverse upland terrestrial ecosystems. Given the high microscale spatial heterogeneity, the soil redox conditions inferred from Mn oxidation states in bulk soil are averaged values incorporating both macro- and microsites of variable redox conditions. Effective water balance (MAP–PET), calculated as MAP minus potential evapotranspiration (PET), serves as our proxy for the long-term average site-specific water balance. This calculated climatic factor is well-correlated with average soil moisture and organic carbon content (See below).

We analyzed bulk soil samples (top 30 cm) using chemical extractions (Methods) from 37 terrestrial sites (3 replicates at each site) within the U.S. National Ecological Observatory Network

(NEON), strategically spanning 20 ecoclimatic domains[20] (Fig. 1). All NEON soils were collected at peak growing season. We further supplemented the NEON soils with eight Hawaiian soils (no replicates) reported previously[13] to expand the range of MAP–PET (Fig. 1). The extractions isolated the redox actively cycled Mn fractions, including $MgCl_2$-extracted Mn to represent Mn(II), pyrophosphate-extracted Mn minus $MgCl_2$-extracted Mn to approximate Mn(III), and $NH_2OH{\cdot}HCl$-extracted Mn as Mn(IV) (Methods). This extraction protocol excludes extractions of relatively inert Mn species, such as those in parent minerals which are not responsive to redox fluctuations in a short term. Thus, these chemical extractions are more suitable than X-ray spectroscopic analysis that probes the entire Mn pool in soils[13] for our goal of an active redox proxy. For Hawaiian samples previously shown by spectroscopy to contain only Mn(II) in the total Mn pool, we used the spectroscopic speciation directly. The resulting dataset comprises 45 study sites and 159 individual samples covering a broad range of effective water balance. We compared multiple PET modeling methods and found similar patterns in Mn oxidation states relative to effective water balance, though specific patterns varied slightly by method. Here, we primarily report results obtained via the MODIS16 method (MAP–PET: -2.5 to 1.7 m; Fig. 1), which is particularly useful for predicting soil moisture[21]. We then constructed a MAP–PET-based redox ladder and estimated the global cumulative SOC stock that is influenced by either oxic, suboxic, or anoxic soil conditions.

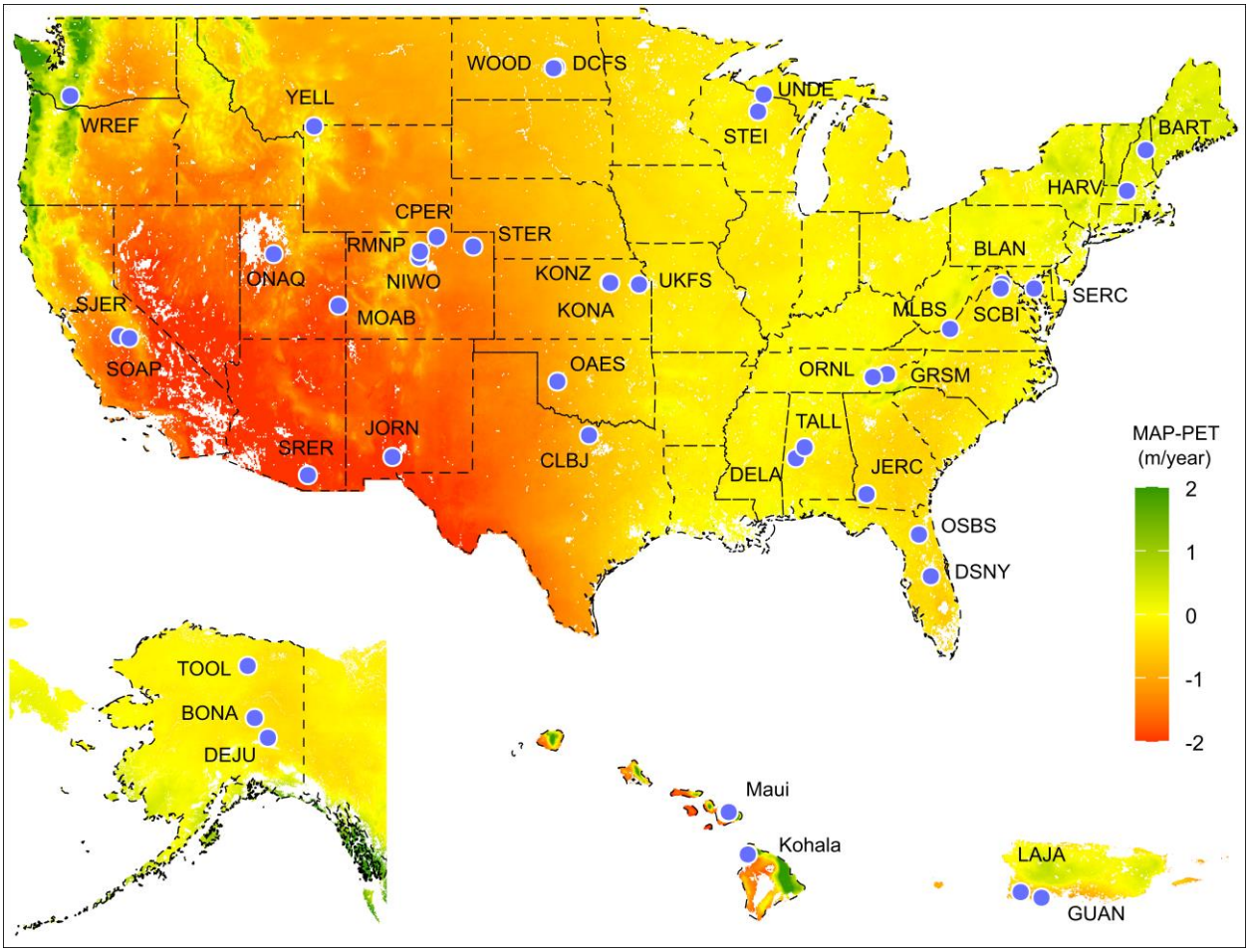

Fig. 1 | Study sites span a continental effective water-balance gradient (MAP–PET). Points in blue indicate soil sampling locations across 37 NEON terrestrial sites (three replicates per site; site codes in uppercase). Maui and Kohala sites on the Hawaiian Islands (eight soils in total) were to extend the effective water-balance range. The background raster shows long-term effective water balance (MAP–PET; m yr^{-1}), calculated as mean annual precipitation (MAP) averaged from TerraClimate precipitation (2000–2020)[22] minus mean annual potential evapotranspiration (PET) averaged from the MOD16 PET product (2000–2020)[23]. MAP–PET is used here as a proxy for spatial variation in long-term effective soil moisture.

Continental-scale pattern of Mn oxidation states and soil redox conditions

The oxidation states of Mn in the active soil Mn pool exhibit a clear dependence on water balance conditions, despite considerable soil/vegetation variability across the continental-scale dataset. The fractions of Mn oxidation states predominantly vary within a MAP–PET range of approximately -1 to 1 m (Fig. 2). Mn(IV) dominates under drier conditions (MAP–PET < -1 m), decreasing sharply as conditions become wetter (MAP–PET approaching 1 m; Fig. 2c). Conversely, Mn(II) exhibits an inverse pattern, increasing significantly as conditions transition from dry to wet (Fig. 2a). Mn(III), intermediate in oxidation state, reaches its peak near neutral effective water balance (MAP–PET ~0 m; Fig. 2b). Similar patterns were obtained when PET was estimated using alternative methods although the threshold values shifted slightly (Extended Data Figure 1), supporting the robustness of these trends.

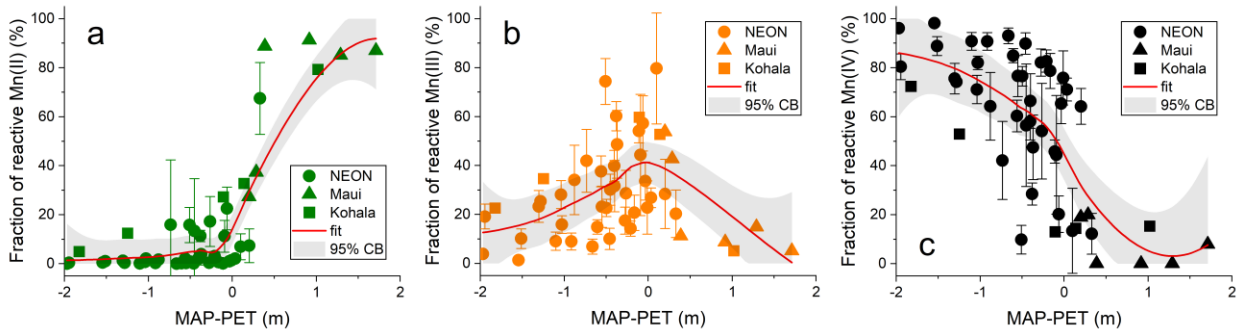

Fig. 2 | Variations of Mn oxidation states in actively cycled pools in soils across effective water balance (MAP–PET). a-c, the relative fractions of actively cycled Mn(II) (**a**), Mn(III) (**b**), and Mn(IV) (**c**) as a function of MAP–PET. Fractions were fitted using a nonparametric local regression (red lines). The gray bands represent the 95% confidence intervals. MAP: mean annual precipitation, PET: mean annual potential evapotranspiration. The PET data were estimated according to the MOD16 method.

Based on the established relationships between dominant Mn oxidation states and redox conditions, we delineate three distinct characteristic soil redox regimes: oxic at MAP–PET < -1 m and dominated by Mn(IV); suboxic at -1 m < MAP–PET < 1 m and characterized by the co-existence of Mn(II), Mn(III) and Mn(IV) and peak Mn(III); and anoxic at MAP–PET > 1 m and dominated by Mn(II). The peak Mn(III) fraction notably marks the center of the suboxic regime. The onset of Mn(II) accumulation and Mn(IV) depletion marks the transition from net average oxic to suboxic conditions, while complete dominance of Mn(II) and depletion of Mn(IV) define the net anoxic regime (Fig. 2). Thus, effective water balance systematically organizes these upland soils into a net average oxic-suboxic-anoxic redox gradient, and the characteristic soil redox conditions became increasingly reducing as the moisture increases.

As noted above, soil pH can influence Mn oxidation states, but our NEON dataset indicates that redox conditions are the dominant control on Mn oxidation state. An analysis using structural equation modeling (SEM) shows that pH plays a weaker, negative role in the relative abundance of reduced Mn species (%Mn(II)) than other factors, particularly SOC and soil water content (Fig. 3). The two variables primarily influence Mn oxidation states through their effects on O_2 dynamics, as discussed below. Previous studies have often attributed elevated Mn(II) in acidic soils solely to low pH[24], overlooking the co-occurring reducing environments that develop where organic matter and soil moisture are abundant. Although pH has a recognized role in constraining the stability of Mn species, the MAP–PET thresholds we propose here based on Mn oxidation states more effectively capture distinct redox regimes.

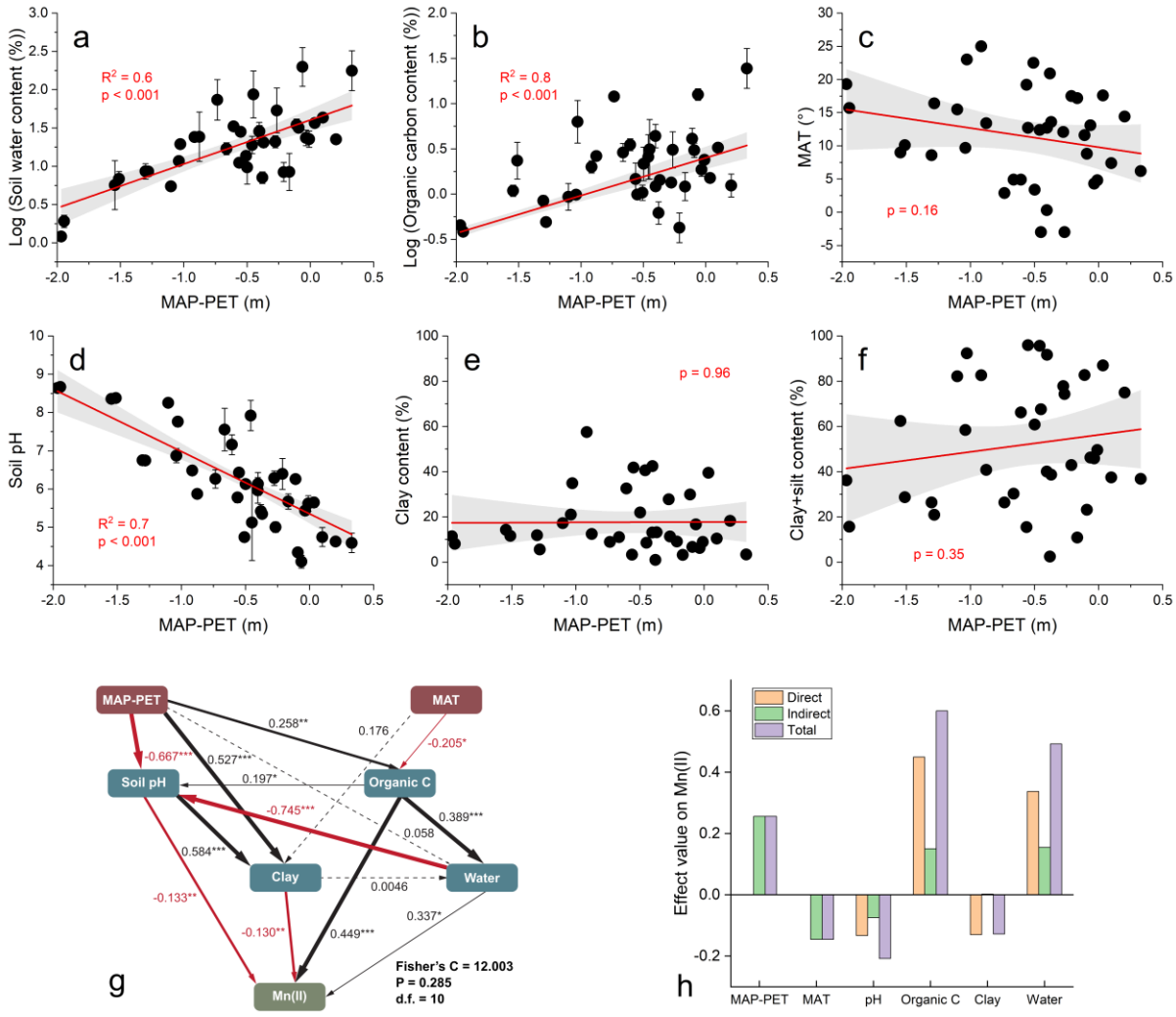

Fig. 3 | Environmental controls on the actively cycled Mn(II) fraction across an effective water-balance gradient (MAP–PET). **a–f,** Relationships between effective water balance (MAP–PET) and key soil/climate variables: log-transformed soil water content (**a**), log-transformed soil organic carbon content (**b**), mean annual temperature (MAT; c), soil pH (**d**), clay content (**e**), and fine fraction (clay + silt; **f**). **g**, Structural equation model (SEM) summarizing the direct and indirect effects of MAP–PET, MAT, and soil properties on the fraction of the actively cycled Mn pool present as Mn(II). **h**, Standardized direct, indirect, and total effects on Mn(II) fraction derived from the SEM. In **a–f**, red lines show least-squares linear fits and shaded bands indicate 95% confidence intervals. In g, arrows denote significant pathways ($P < 0.05$); black and red arrows indicate positive and negative relationships, respectively, and arrow width scales with effect strength. Numbers on arrows are standardized path coefficients (*$P < 0.05$, **$P < 0.01$, ***$P < 0.001$). MAP, mean annual precipitation; PET, mean annual potential evapotranspiration.

Characteristic soil redox state emerges from climate-driven SOC and moisture controls

Higher effective water balance (MAP–PET) is associated with more reducing soils across the NEON sites, as reflected by lower Mn oxidation states (i.e., higher %Mn(II), Fig. 2). This pattern primarily arises because MAP–PET strongly controls SOC and soil moisture: both increase approximately exponentially with MAP–PET (Fig. 3 a,b; log y axes). The SEM analysis further suggests that SOC and soil water content exert strong, positive direct effects on %Mn(II) (Fig. 3h). Mechanistically, high SOC fuels microbial respiration that consumes O_2, while diffusion of O_2 into waterfilled pores is inherently slow.

Mean annual temperature and clay content influence redox conditions but play secondary roles (Fig. 3h). Although higher temperature generally accelerates microbial metabolism and thus O_2 demand, in our dataset MAT shows a weaker, net negative association with anaerobiosis. A plausible mechanism is that higher MAT raises PET, drying soils and suppressing reducing conditions (Fig. 3c), as exemplified by the warm, arid Jornada Basin site of NEON (the site denoted JORN in Fig. 1). Our measurements suggest that increased temperature alone does not enhance reducing conditions; it acts jointly with SOC and moisture to produce a warm, moist, organic-rich environment conducive to anaerobiosis. The negative, albeit weaker, effect of clay on reducing conditions is likewise counterintuitive. Clay-rich soils lengthen gas-diffusion pathways and retain more water, which should restrict O_2 supply[25]. However, fine-textured soils also stabilize organic carbon as mineral-associated organic matter, limiting substrate availability for microbial respiration and thereby lowering O_2 demand. By contrast, clay-poor soils contain relatively unprotected, labile organic matter, such as particulate organic matter, that fuels rapid respiration[26]. The observed negative association between clay content and %Mn(II) (Fig. 3g)

therefore suggests that the net clay-induced variation in O_2 demand outweighs variation in O_2 supply in governing redox status, consistent with a recent study in a grassland[27].

Climate-driven redox ladder across upland ecosystems

The distribution of redox conditions and the dominant terminal electron acceptors (TEAs) for SOC decomposition in global upland ecosystems can be described by a redox ladder governed by MAP–PET (Fig. 4a). A redox ladder conceptually arranges respiratory pathways by decreasing energy yield of the TEA. In wetlands, such ladders typically track flooding duration or soil depth. In uplands, MAP–PET plays an analogous role by regulating water and organic C content that in turn control O_2 dynamics. Considering the position of Mn on this ladder, we infer that as climate becomes drier, dominant TEAs in upland soils shift sequentially from O_2 to nitrate, to Mn(III/IV) oxides, and then to Fe(III). Thus, MAP–PET systematically establishes a clear redox gradient across upland environments (Fig. 4a).

This climate-driven ladder aligns with established redox boundaries from prior work. Only the two wettest sites of the Maui rainfall gradient with MAP–PET > 1.3 m show extensive Fe(III) reduction[28]. For another example, Calabrese et al.[29] calculated minimal monthly occurrence of potential anoxia (<5%) and limited Fe(III) reduction at a subtropical forest (Calhoun, South Carolina; MAP–PET = 0.45 m), but substantially greater potential anoxia (15 – 40% monthly occurrence) and extensive Fe(III) reduction in a humid tropical forest (Luquillo, Puerto Rico; MAP–PET = 2.4 m).

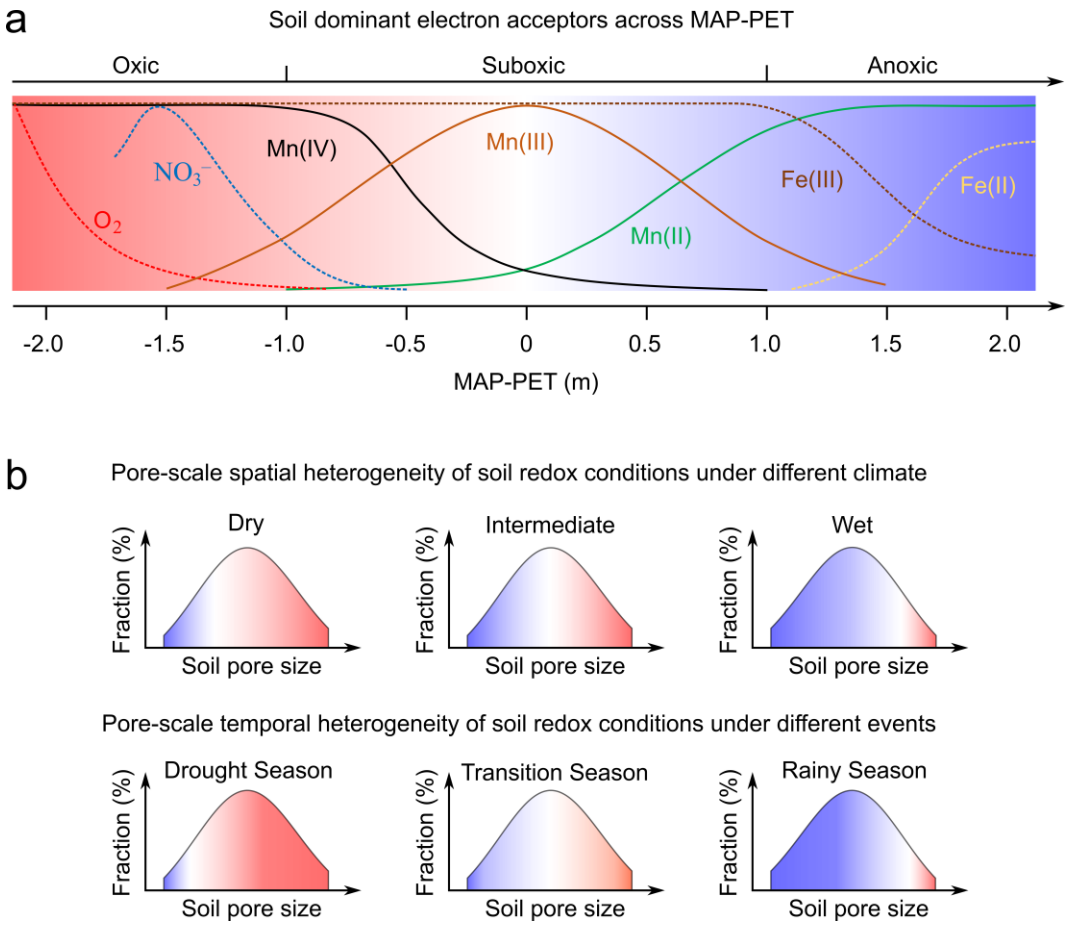

Fig. 4 | Conceptual redox ladder and pore-scale heterogeneity along an effective water-balance gradient (MAP–PET). a, Conceptual model of dominant terminal electron acceptors for organic matter oxidation in upland soils along the MAP–PET gradient. With increasing MAP–PET, the dominant electron acceptor shifts sequentially from O_2 to NO_3^-, then to Mn(III/IV) oxides, and finally to Fe(III) oxides, reflecting progressive oxidant depletion during microbial respiration (analogous to redox zonation with depth in wetland profiles). O_2 and NO_3^- are primarily dissolved in soil pore water, whereas Mn and Fe species occur mainly as solid phases (sorbed ions or mineral constituents). Sulfate reduction is not shown because it is typically restricted to persistently waterlogged or submerged soils[2]. **b**, Schematic of pore-scale redox heterogeneity across climates and events. Soil structure creates redox microenvironments in which macropores can be rapidly re-oxygenated during wetting/drainage, whereas diffusion-limited micropores may remain anoxic even when bulk soils are relatively dry, generating both spatial (dry–intermediate–wet) and temporal (drought–transition–rainy season) redox variability. MAP, mean annual precipitation; PET, potential evapotranspiration[1,2].

Soil pore-scale heterogeneity and its impacts on soil redox state

Our analysis integrates redox conditions across pore scales. Macropores and micropores often differ markedly in O_2 content, with micropores typically more reducing, especially in moist soils, so that anoxic micropores can coexist with oxic macropores in uplands. Microporosity arises not only from clays but also from the architecture of particulate organic matter. Conventional E_h measurements with Pt electrodes may disproportionately reflect macropore conditions. For example, Pt-electrode E_h values from Maui soils span oxic to anoxic regimes[13], whereas our bulk Mn oxidation-state data show a stronger skew toward suboxic to anoxic conditions (Fig. 2). We therefore suggest that Mn oxidation states of bulk soils better integrate redox across both macropores and the less-oxygenated micropore domain.

While Mn oxidation states provide a tractable, integrative proxy for bulk redox status across soil pores of various sizes, they cannot capture the full spatial heterogeneity of soil redox conditions. Within soils that are characteristically suboxic, some microsites can be deeply anoxic, as conceptually depicted in Fig. 4b, triggering anaerobic reduction of Fe(III), sulfate, or even CO_2 to produce methane. Conversely, oxic macropores can occur within characteristically anoxic soils (Fig. 4b) where Fe(III) reduction is prevalent. In addition to spatial heterogeneity, soil redox conditions have a strong temporal fluctuation (Fig. 4b). Nevertheless, Mn oxidation states meaningfully integrate across pore domains and sites, offering a useful indicator of average ecosystem-scale redox environments.

Oxygen limitation reshapes global soil organic carbon stabilization

Oxygen limitation is a pivotal yet often overlooked control on the persistence of SOC in upland ecosystems[1,2,12,30]. Although oxygen scarcity is most commonly framed as a wetland

phenomenon, our dataset indicates that ~78 – 91% of global SOC resides in soils with characteristic suboxic conditions and a further ~5 – 9% in anoxic soils (Extended Data Figure 2). This distribution implies that restricted O_2 availability rather than mineral protection alone[11] can constrain SOC decomposition across much of the land surface, even though transient redox oscillations can accelerate mineralization[31]. It also suggests a self-reinforcing protection mechanism: labile SOC fuels microbial respiration that consumes O_2, deepening reducing conditions and further suppressing decomposition.

The strength of this constraint depends on the terminal electron acceptors available in each redox regime. Mn-oxide concentrations in soils are typically low (600 – 1,000 mg kg^{-1}) and therefore seldom sustain extensive oxidative decomposition beyond the litter layer[32], leaving SOC relatively well protected under suboxic conditions from the perspective redox constraints. By contrast, ferric iron [Fe(III)] is abundant, even in anoxic upland soils, providing a potent electron acceptor that can support substantial carbon oxidation despite O_2 scarcity[29]. Consequently, SOC in suboxic horizons where most upland carbon resides, likely has greater protection than SOC in anoxic zones rich in Fe.

Redox conditions are highly sensitive to climate and land-management change. Shifts in precipitation patterns, including more frequent extremes, alter soil water balance; prolonged drought drives soils toward more oxic states and accelerates carbon loss. Suboxic soils likely respond most strongly to these climate dynamics, as suggested by steep changes in Mn oxidation states along the MAP–PET gradient (Extended Data Figure 2). Land-use practices such as tillage aerate surface soils and increase decomposition, with the greatest losses expected in humid regions where baseline O_2 limitation is strongest[33].

Finally, effective water balance is a powerful climatic predictor of soil properties linked to SOC stabilization. Soil redox status, pH[34], and the concentration of dissolved organic carbon associated with secondary minerals[11] all vary systematically with MAP–PET in ways that favor SOC stabilization, with pronounced transitions near hydrologic balance (MAP–PET ≈ 0). We therefore recommend explicitly representing soil O_2 status in upland soils in ecosystem models to improve predictions of SOC responses under future climate scenarios.

Acknowledgments

This work was supported by National Science Foundation under DEB-2027284. The National Ecological Observatory Network (NEON) is a program sponsored by the U.S. National Science Foundation and operated under cooperative agreement by Battelle.

Author contributions

K.W. collected and analyzed experimental data. E.S. developed the MAP and PET models and quantified organic-carbon stocks. H.L. performed the SEM analysis. M.Z. and K.W. conceived the study, developed the conceptual framework and designed the methodology. O.A.C. contributed to conceptual development. K.W. and M.Z. wrote the manuscript with input from all authors. All authors interpreted the data and contributed to the discussion and final manuscript.

Methods

Study sites and soil pretreatments. National Ecological Observatory Network (NEON) comprises 47 terrestrial sites strategically distributed across 20 ecoclimatic domains in the U.S., representing the regions of distinct landforms, vegetation, climate, and ecosystem dynamics, capturing the broad ecological and climatic diversity of the U.S.[20]. In this study, 37 NEON sites were selected (Fig. 1), encompassing forest, grassland, shrubland, and cultivated landcover types. At each site, soil samples were collected by NEON from up to 30 cm depth at three different

random locations within a 40 m × 40 m plot, yielding a total of 120 soil samples. Soils were broadly classified by NEON as originating from organic or mineral horizons, with most samples in this study derived from mineral horizons. Soil samples were stored at -80°C at the NEON Biorepository at Arizona State University. Prior to further characterizations, samples were thawed, gently homogenized after removal of visible plant debris, and then refrozen to maintain moisture consistency. Additionally, two well-documented model ecosystem sites from the Hawaiian Islands, i.e., Maui and Kohala sites, were included in the present study[13,35,36]. Detailed protocols for soil collection and pretreatment at these sites have been described previously[7,13,37]

Soil texture estimation. Due to limited soil sample material availability, soil texture was not directly measured. However, as the NEON soils (0 – 30 cm) were collected from the same sites as the NEON archived Megapit soils, the soil texture was estimated using the Megapit soil profile data. For the Megapit soils, the soil texture (fractions of sand, silt, and clay) was determined and reported for each genetic horizon. These fractions were then integrated to a depth of 30 cm based on horizon thickness and soil bulk density, giving the estimated soil texture of the studied soils.

Measurement of carbon and nitrogen content. The total carbon and nitrogen content in the NEON soils was determined using a Costech 4010 elemental analyzer equipped with a thermal conductivity detector. Data were processed using the EAS32 software. To quantify soil organic carbon, soil inorganic carbon was removed via an acid fumigation procedure[38]. Briefly, 150 mg of well-homogenized and finely-ground soil was weighed into a 20-mL glass scintillation vial and moistened by 150 μL of deionized water. The vials were placed in a vacuum desiccator along with a beaker containing 200 mL of 12 mol/L concentrated HCl. The desiccator was sealed under a vacuum of 80 kPa, and the samples were exposed to HCl vapor for 72 h. Thereafter, residual HCl vapor was removed by repeated evacuation under vacuum. The soil samples were then oven-dried, reground into fine powders, analyzed for organic carbon content.

Chemical extraction of the active soil Mn pool. Two chemical extraction methods were employed to assess the active Mn pool in soils: sequential extraction and pyrophosphate (PP) extraction. Sequential extraction was used to quantify functional Mn fractions (pools) in the NEON soils, whereas PP extraction was used to semi-quantify Mn(III) in conjunction with the exchangeable Mn(II) pool determined via sequential extraction. PP extracts Mn(III) complexed with organic matter[19,39], and Mn(III) in the structure of poorly crystalline Mn and Fe oxides that can be partially dissolved in PP solution[40–42]. In addition to Mn(III), PP can also extract

316 exchangeable Mn(II), due to the high concentration of Na^+ in the sodium pyrophosphate reagent
317 and the weak complexation between PP and Mn(II). Therefore, Mn(III) was calculated as the
318 difference between the PP-extracted Mn and the exchangeable Mn(II) measured in the sequential
319 extractions.

320 The sequential extraction was conducted following the method of Tessier et al.[43], with
321 modifications to account for Mn incorporated into the structure of Fe oxides. Approximately 0.2 g
322 (dry weight equivalent) of frozen NEON soils was placed into a 15-mL polypropylene centrifuge
323 tube, followed by addition of the extraction solution. After each extraction step, the mixture was
324 centrifuged at 5000 r/min for 30 min and filtered through a 0.22 μm membrane. The filtrates were
325 diluted and acidified prior to ICP-OES analysis. Detailed experimental conditions and procedures
326 are summarized in Extended Data Table 1. Six major Mn pools were defined: (1) exchangeable
327 Mn, (2) Mn carbonates and Mn sorbed on mineral surfaces, (3) Mn oxides, (4) Mn complexed with
328 organic matter, (5) Mn incorporated into the structure of Fe oxides, and (6) Mn in the residue. The
329 sum of the first five fractions represents the active Mn pool.

330 For PP extraction, approximately 0.2 g (dry weight equivalent) of frozen NEON soil was
331 mixed with 4 mL of 1 mol/L sodium pyrophosphate solution in a 15-mL centrifuge tube. The soil
332 suspension was shaken for 16 h at room temperature and then processed following the same
333 centrifugation and filtration steps as in the sequential extraction.

334 In the sequential extraction, exchangeable Mn primarily presents as Mn(II), while extracted
335 Mn oxides consist mainly of Mn(IV). Thereby, the acquired data provide estimates of the relative
336 proportions of active Mn(II) and Mn(IV) pools in soils. PP extraction targets both active Mn(II)
337 and Mn(III), including Mn(III) oxyhydroxides. By subtracting the exchangeable Mn(II) measured
338 in the sequential extraction from the total Mn extracted by PP, the relative proportion of active
339 Mn(III) in soils can be estimated. Combining these three active Mn pools—Mn(II), Mn(III), and
340 Mn(IV)—allows calculation of the relative abundance of each Mn oxidation state, as well as the
341 average Mn oxidation state (AOS) of the active Mn pool.

342 **Climate data.** Climate data for the study sites were obtained from multiple sources. For
343 the NEON sites across North America, global-scale products were used, while locally resolved
344 data were applied for the Hawaiian sites. Where available, data from the 24 months prior soil
345 sampling were averaged. Mean annual precipitation (MAP) for the NEON sites was extracted from
346 TerraClimate[44], except for sites in Puerto Rico, for which the higher-resolution DayMet

climatology was used[45]. MAP for the Hawaiian sites was sourced from the Hawai'i rainfall atlas[46].

Potential evapotranspiration (PET) was estimated using several methods. First, PET was derived from the MOD16 evapotranspiration algorithm, which integrates multiple remote-sensing inputs at relatively high spatial resolution. For the NEON sites, MOD16 PET values were extracted and averaged over the 24 months before sampling. For the Hawaiian sites, where samples were collected in the 1990s (pre-dating MOD16 availability), PET was averaged over 2001–2010.

The MOD16 PET estimate incorporates a potential canopy evaporation term, differing from conventional PET formulations. To evaluate the sensitivity of our results to the PET model, two additional PET estimates were generated and compared. The first alternative followed the modified Penman–Monteith approach described by in Slessarev et al.[34], which integrates remotely sensed leaf area index (LAI) and surface energy balance terms. Our implementation closely followed theirs but used climate inputs appropriate to our spatial scale. For the NEON sites, monthly mean air temperature and vapor pressure deficit were taken from TerraClimate [44]; LAI from the GLASS LAI product (0.1° resolution)[47]; Land cover from MCD12[48]; radiation from CERES[49]; and air pressure was calculated from elevation using the GMTED2010 digital elevation model[50]. For the Hawaiian sites, equivalent inputs were obtained from the Hawaii Climate Data Portal[46]. PET for the Hawaii sites was averaged over 2001-2010 due to lack of earlier input data. The second alternative applied the Hargreaves reference evapotranspiration method, which estimates ET from a well-watered grass surface using mean air temperature and shortwave downwelling radiation[51]. Required inputs were obtained from TerraClimate and CERES for the NEON sites, and from the Hawaii Climate Data Portal for the Hawaii sites. Daily PET (mm) was calculated as:

$$PET_{Hargreaves}=0.135\times\frac{SWD}{\lambda}\times(T_{air}+17.8)$$

Where SWD is the incident shortwave radiation (MJ m^{-2} d^{-1}), λ is the latent heat of vaporization of water (2.45 MJ kg^{-1}), and T_{air} is the air temperature (°C).

Structural equation modeling. Prior to constructing the structural equation model (SEM), multicollinearity among environmental variables were assessed by calculating variance inflation factor (VIF) using the "car" package in R. Variables with VIF > 5 were excluded to reduce multicollinearity. Next, backward stepwise regression was performed using the "MASS" package in R to identify significant predictors of soil Mn(II) relative abundance. Finally, an SEM was built using the "piecewiseSEM" package in R to evaluate both indirect effects of climatic factors (MAP-

PET and MAT) and direct effects of soil physicochemical properties (pH, organic carbon concentration, clay content, and soil water content) on the relative abundance of soil Mn(II).

Global soil organic carbon distribution in relation to climate. A cumulative distribution function for soil organic carbon (SOC) with climate was constructed using the Harmonized World Soil Database (HWSD) combined with the MAP and PET data described above. We employed a re-gridded, 0.05°-resolution estimate of topsoil (0-30 cm) SOC storage from HWSD[52]. To reduce computational demands, calculations were performed on a random sample of 100,000 grid cells from the HWSD. For each sampled cell center, precipitation, air temperature, and vapor pressure deficit data were extracted from TerraClimate for the period 2001-2010. MOD16 PET data for the same period were also extracted and averaged. To calculate PET using the Slessarev (2016)[34] and Hargreaves methods[51], we additionally gathered CERES radiation fluxes, leaf area index, land cover, and elevation data from the sources noted earlier.

The cumulative SOC as a function of MAP–PET was derived through the following steps: (1) total SOC storage per grid cell was calculated by multiplying the SOC stock by the cell area, adjusted as a function of latitude; (2) cells were grouped into 50-mm bins based on MAP–PET values, spanning a range from –2500 mm to +10,000 mm; (3) total SOC within each bin was summed and then cumulated from the lowest to the highest MAP–PET values; (4) cumulative SOC per bin was expressed as a proportion of the grand total SOC across all sampled cells. MAP was averaged from TerraClimate for the period 2001-2010.

Reference

1. Keiluweit, M., Wanzek, T., Kleber, M., Nico, P. & Fendorf, S. Anaerobic microsites have an unaccounted role in soil carbon stabilization. *Nat Commun* **8**, 1771 (2017).
2. Lacroix, E. M. *et al.* Consider the Anoxic Microsite: Acknowledging and Appreciating Spatiotemporal Redox Heterogeneity in Soils and Sediments. *ACS Earth Space Chem.* **7**, 1592–1609 (2023).
3. Meng, D. *et al.* Effects of redox potential on soil cadmium solubility: Insight into microbial community. *Journal of Environmental Sciences* **75**, 224–232 (2019).
4. Zhang, Z. & Furman, A. Soil redox dynamics under dynamic hydrologic regimes - A review. *Science of The Total Environment* **763**, 143026 (2021).
5. Husson, O. Redox potential (Eh) and pH as drivers of soil/plant/microorganism systems: a transdisciplinary overview pointing to integrative opportunities for agronomy. *Plant Soil* **362**, 389–417 (2013).
6. Pett-Ridge, J. & Firestone, M. K. Redox Fluctuation Structures Microbial Communities in a Wet Tropical Soil. *Appl Environ Microbiol* **71**, 6998–7007 (2005).
7. Schuur, E. A. G., Chadwick, O. A. & Matson, P. A. Carbon cycling and soil carbon storage in mesic to wet hawaiian montane forests. *Ecology* **82**, 3182–3196 (2001).
8. Fiedler, S., Vepraskas, M. J. & Richardson, J. L. Soil Redox Potential: Importance, Field Measurements, and Observations. in *Advances in Agronomy* vol. 94 1–54 (Elsevier, 2007).
9. Stolze, L. *et al.* Climate forcing controls on carbon terrestrial fluxes during shale weathering. *Proc. Natl. Acad. Sci. U.S.A.* **121**, e2400230121 (2024).
10. Wilmoth, J. L. Redox Heterogeneity Entangles Soil and Climate Interactions. *Sustainability* **13**, 10084 (2021).
11. Kramer, M. G. & Chadwick, O. A. Climate-driven thresholds in reactive mineral retention of soil carbon at the global scale. *Nature Clim Change* **8**, 1104–1108 (2018).

12. Lacroix, E. M., Mendillo, J., Gomes, A., Dekas, A. & Fendorf, S. Contributions of anoxic microsites to soil carbon protection across soil textures. *Geoderma* **425**, 116050 (2022).
13. Wen, K. *et al.* Manganese Oxidation States in Volcanic Soils across Annual Rainfall Gradients. *Environ. Sci. Technol.* **57**, 730–740 (2023).
14. Trouwborst, R. E., Clement, B. G., Tebo, B. M., Glazer, B. T. & Luther, G. W. Soluble Mn(III) in Suboxic Zones. *Science* **313**, 1955–1957 (2006).
15. Madison, A. S., Tebo, B. M., Mucci, A., Sundby, B. & Luther, G. W. Abundant Porewater Mn(III) Is a Major Component of the Sedimentary Redox System. *Science* **341**, 875–878 (2013).
16. Rabenhorst, M. C. *et al.* Manganese-coated IRIS to document reducing soil conditions. *Soil Science Soc of Amer J* **85**, 2201–2209 (2021).
17. Zhang, Z. *et al.* Manganese oxidation states and availability in forest weathering profiles of contrasting climate. *Geochimica et Cosmochimica Acta* **388**, 221–235 (2025).
18. Paulus, E. L. & Vitousek, P. M. Manganese and soil organic carbon stability on a Hawaiian grassland rainfall gradient. *Soil Biology and Biochemistry* **194**, 109418 (2024).
19. Jones, M. E. *et al.* Manganese-Driven Carbon Oxidation at Oxic–Anoxic Interfaces. *Environ. Sci. Technol.* **52**, 12349–12357 (2018).
20. Thorpe, A. S. *et al.* Introduction to the sampling designs of the N ational E cological O bservatory N etwork T errestrial O bservation S ystem. *Ecosphere* **7**, e01627 (2016).
21. Brust, C. *et al.* Using SMAP Level-4 soil moisture to constrain MOD16 evapotranspiration over the contiguous USA. *Remote Sensing of Environment* **255**, 112277 (2021).
22. Abatzoglou, J. T., Dobrowski, S. Z., Parks, S. A. & Hegewisch, K. C. TerraClimate, a high-resolution global dataset of monthly climate and climatic water balance from 1958–2015. *Sci Data* **5**, 170191 (2018).
23. Running, S., Mu, Q., Zhao, M. & Moreno, A. MODIS/Terra Net Evapotranspiration Gap-Filled 8-Day L4 Global 500m SIN Grid V061. NASA Land Processes Distributed Active Archive Center https://doi.org/10.5067/MODIS/MOD16A2GF.061 (2021).

24. Foy, C. D., Scott, B. J. & Fisher, J. A. Genetic Differences in Plant Tolerance to Manganese Toxicity. in *Manganese in Soils and Plants* (eds Graham, R. D., Hannam, R. J. & Uren, N. C.) 293–307 (Springer Netherlands, Dordrecht, 1988). doi:10.1007/978-94-009-2817-6_20.
25. Keiluweit, M., Gee, K., Denney, A. & Fendorf, S. Anoxic microsites in upland soils dominantly controlled by clay content. *Soil Biology and Biochemistry* **118**, 42–50 (2018).
26. Benbi, D. K., Boparai, A. K. & Brar, K. Decomposition of particulate organic matter is more sensitive to temperature than the mineral associated organic matter. *Soil Biology and Biochemistry* **70**, 183–192 (2014).
27. Lacroix, E. M. *et al.* Soil carbon concentration drives anoxic microsites across horizons, textures, and aggregate position in a California grassland. *Geoderma* **454**, 117165 (2025).
28. Scribner, A. M., Kurtz, A. C. & Chadwick, O. A. Germanium sequestration by soil: Targeting the roles of secondary clays and Fe-oxyhydroxides. *Earth and Planetary Science Letters* **243**, 760–770 (2006).
29. Calabrese, S., Barcellos, D., Thompson, A. & Porporato, A. Theoretical Constraints on Fe Reduction Rates in Upland Soils as a Function of Hydroclimatic Conditions. *JGR Biogeosciences* **125**, e2020JG005894 (2020).
30. Keiluweit, M., Nico, P. S., Kleber, M. & Fendorf, S. Are oxygen limitations under recognized regulators of organic carbon turnover in upland soils? *Biogeochemistry* **127**, 157–171 (2016).
31. Lin, Y. *et al.* Differential effects of redox conditions on the decomposition of litter and soil organic matter. *Biogeochemistry* **154**, 1–15 (2021).
32. Jones, M. E. *et al.* Enzymes, Manganese, or Iron? Drivers of Oxidative Organic Matter Decomposition in Soils. *Environ. Sci. Technol.* **54**, 14114–14123 (2020).
33. Six, J., Elliott, E. T., Paustian, K. & Doran, J. W. Aggregation and Soil Organic Matter Accumulation in Cultivated and Native Grassland Soils. *Soil Science Soc of Amer J* **62**, 1367–1377 (1998).
34. Slessarev, E. W. *et al.* Water balance creates a threshold in soil pH at the global scale. *Nature* **540**, 567–569 (2016).

35. *Biogeochemistry of the Critical Zone*. (Springer International Publishing, Cham, 2022). doi:10.1007/978-3-030-95921-0.
36. Paulus, E. L. & Vitousek, P. M. Manganese and soil organic carbon stability on a Hawaiian grassland rainfall gradient. *Soil Biology and Biochemistry* **194**, 109418 (2024).
37. Miller, A. J., Schuur, E. A. G. & Chadwick, O. A. Redox control of phosphorus pools in Hawaiian montane forest soils. *Geoderma* **102**, 219–237 (2001).
38. Ramnarine, R., Voroney, R. P., Wagner-Riddle, C. & Dunfield, K. E. Carbonate removal by acid fumigation for measuring the δ^{13} C of soil organic carbon. *Can. J. Soil. Sci.* **91**, 247–250 (2011).
39. Oldham, V. E., Mucci, A., Tebo, B. M. & Luther, G. W. Soluble Mn(III)–L complexes are abundant in oxygenated waters and stabilized by humic ligands. *Geochimica et Cosmochimica Acta* **199**, 238–246 (2017).
40. Rennert, T. Wet-chemical extractions to characterise pedogenic Al and Fe species – a critical review. *Soil Research* **57**, 1–16 (2019).
41. Wang, Y. & Stone, A. T. Phosphonate- and Carboxylate-Based Chelating Agents that Solubilize (Hydr)oxide-Bound Mn^{III}. *Environ. Sci. Technol.* **42**, 4397–4403 (2008).
42. Klewicki, J. K. & Morgan, J. J. Dissolution of β-MnOOH particles by ligands: pyrophosphate, ethylenediaminetetraacetate, and citrate. *Geochimica et Cosmochimica Acta* **63**, 3017–3024 (1999).
43. Tessier, A., Campbell, P. G. C. & Bisson, M. Sequential extraction procedure for the speciation of particulate trace metals. *Anal. Chem.* **51**, 844–851 (1979).
44. Abatzoglou, J. T., Dobrowski, S. Z., Parks, S. A. & Hegewisch, K. C. TerraClimate, a high-resolution global dataset of monthly climate and climatic water balance from 1958–2015. *Sci Data* **5**, 170191 (2018).
45. Thornton, P. E. *et al.* DaymetDaymet: Daily Surface Weather Data on a 1-km Grid for North America, Version 3. 0 MB Preprint at https://doi.org/10.3334/ORNLDAAC/1328 (2016).
46. Longman, R. J. *et al.* High-Resolution Gridded Daily Rainfall and Temperature for the Hawaiian Islands (1990–2014). *Journal of Hydrometeorology* **20**, 489–508 (2019).

47. Liang, S. *et al.* The Global Land Surface Satellite (GLASS) Product Suite. *Bulletin of the American Meteorological Society* **102**, E323–E337 (2021).
48. Sulla-Menashe, D., Gray, J. M., Abercrombie, S. P. & Friedl, M. A. Hierarchical mapping of annual global land cover 2001 to present: The MODIS Collection 6 Land Cover product. *Remote Sensing of Environment* **222**, 183–194 (2019).
49. Doelling, D. CERES Energy Balanced and Filled (EBAF) TOA Monthly means data in netCDF Edition4.1. NASA Langley Atmospheric Science Data Center Distributed Active Archive Center https://doi.org/10.5067/TERRA-AQUA/CERES/EBAF-TOA_L3B004.1 (2019).
50. Danielson, J. J. & Gesch, D. B. *Global Multi-Resolution Terrain Elevation Data 2010 (GMTED2010)*. (2011) doi:10.3133/ofr20111073.
51. George H. Hargreaves & Zohrab A. Samani. Reference Crop Evapotranspiration from Temperature. *Applied Engineering in Agriculture* **1**, 96–99 (1985).
52. Wieder, W. R., Boehnert, J., Bonan, G. B. & Langseth, M. Soil CollectionRegridded Harmonized World Soil Database v1.2. 48.6861 MB Preprint at https://doi.org/10.3334/ORNLDAAC/1247 (2014).

Extended Data Table 1 | Sequential chemical extractions for Mn in the frozen NEON soils.

Experimental condition	Target Mn pool
~ 0.2g dry equivalent frozen soil sample, 4 mL of 1 mol/L $MgCl_2$ solution (pH 7), shaken for 1 h at room temperature	Exchangeable Mn(II)
4 mL of 1 mol/L sodium acetate (pH 5), shaken for 5 h at room temperature	Mn(II) carbonates
10 mL of 0.05 mol/L $NH_2OH{\cdot}HCl$ (in acetic acid, 25% (v/v)), in a water bath at 96°C for 6 h	Mn(IV) oxides
1.5 mL of 0.02 mol/L HNO_3 + 2.5 mL of 30% H_2O_2, pH2, in a water bath at 85°C for 3 h; after cooling, add 2.5 mL of 3.2 mol/L NH_4Ac (in HNO_3 20%(v/v)), and shaken for 30 min at room temperature	Organic complexed Mn
8 mL of 0.3 mol/L sodium citrate + 1 mL of 1 mol/L sodium bicarbonate 30 min at 80°C; then add ~ 1 g sodium dithionite, shaken at 80°C for 30 min	Mn in iron oxides
Residue was generated by subtracting the above fractions from total Mn	Mn in parent materials and occluded Mn(III,IV) oxides

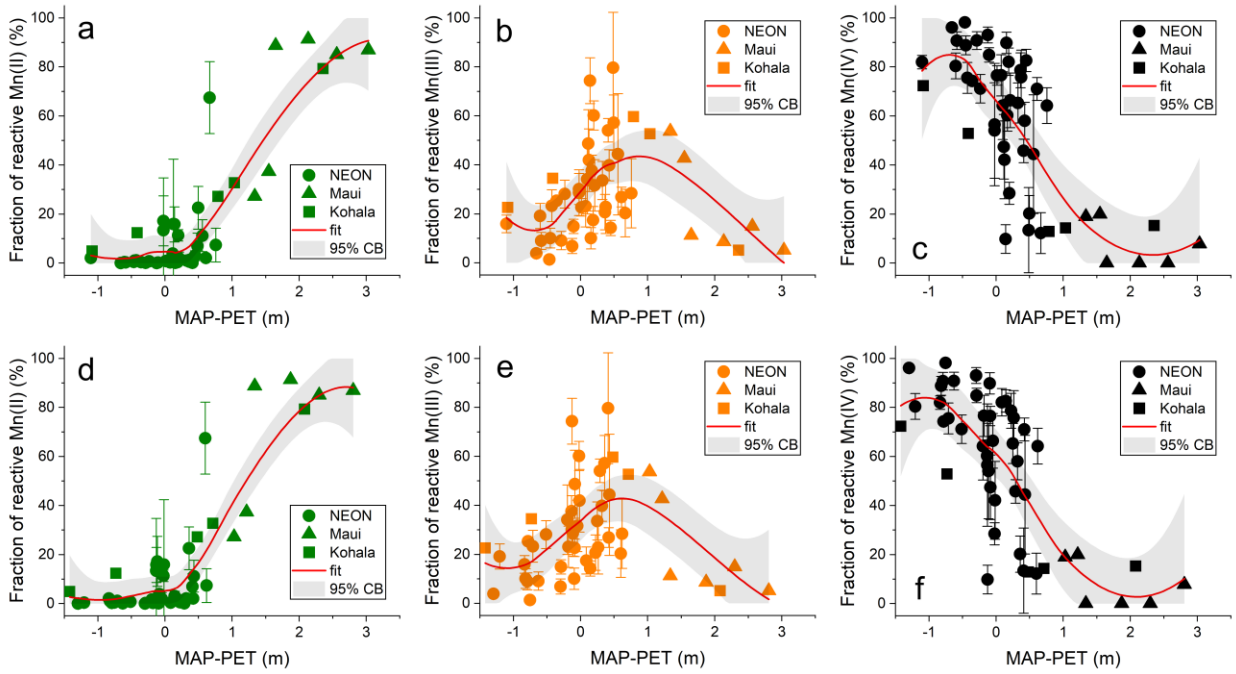

Extended Data Figure 1 | Variations of Mn oxidation states in actively cycled pools across MAP–PET. a-c, The relative fractions of actively cycled Mn(II) (**a**), Mn(III) (**b**), and Mn(IV) (**c**) as a function of MAP–PET, with PET data were estimated according to the modified Penman Montieth (P-M) method; **d-f**, The relative fractions of actively cycled Mn(II) (**d**), Mn(III) (**e**), and Mn(IV) (**f**) as a function of MAP–PET, with the PET data were estimated based on the Hargreaves method. Fractions were quantified by chemical extractions (see Methods) and fitted using a nonparametric local regression (red lines). The gray bands represent the 95% confidence intervals. MAP: mean annual precipitation, PET: mean annual potential evapotranspiration.

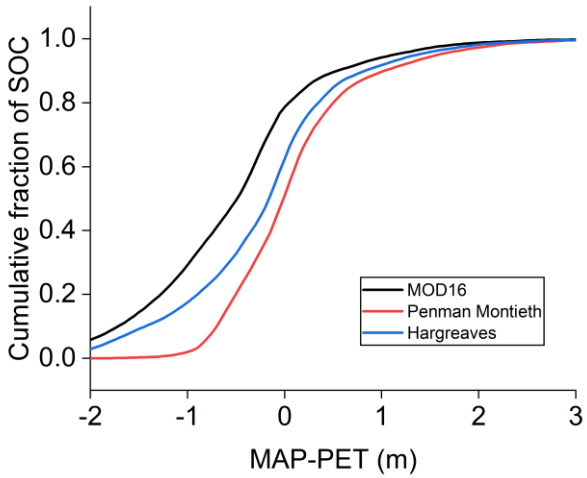

Extended Data Figure 2 | The cumulative global stock of soil organic C in upland soils as a function of effective soil moisture (MAP–PET). The PET data were modeled using the modified Penman Montieth (P-M) method as described in Slessarev[33], Hargreaves method, and MOD16 method. While the P-M method calculated PET values are consistently lower than Hargreaves or MOD16 method, the patterns of the cumulative fraction of SOC versus MAP–PET resemble each other, suggesting the robustness of the pattern.